Radio Science

RESEARCH ARTICLE
10.1029/2018RS006709

Key Points:
- Least squares and maximum likelihood irregularity parameter estimates generate correlated irregularity turbulent strength and spectral index parameter errors
- Such correlations have been incorrectly interpreted as equatorial ionospheric structure characteristics
- An improved maximum likelihood estimation procedure is introduced that reduces the estimated parameter errors to negligible levels

Correspondence to:
C. Rino,
rino@bc.edu

Citation:
Rino, C., & Carrano, C. S. (2018). On the characterization of intermediate-scale ionospheric structure. *Radio Science*, *53*. https://doi.org/10.1029/2018RS006709

Received 8 AUG 2018
Accepted 9 OCT 2018
Accepted article online 15 OCT 2018

On the Characterization of Intermediate-Scale Ionospheric Structure

Charles Rino[1] and Charles Carrano[1]

[1] Institute for Scientific Research, Boston College, Newton, MA, USA

Abstract Characterization of ionospheric structure starts with spectral analysis of one-dimensional time series. Unknown spectral density function (SDF) parameters are estimated by model-fitting procedures, which will be referred to in this paper collectively as irregularity parameter estimation. If the diagnostic SDF has a power law form, linear least squares estimation (LLE) can be used to estimate the power law parameters. In this paper simulations are used to investigate LLE estimates of diagnostic single-component and two-component power law SDFs. There is a known turbulent strength bias and a more troublesome correlation between the turbulent strength and the spectral index. We found that this intrinsic property of LLE estimators completely explains a similar correlation long observed in both in situ and radio propagation ionospheric diagnostic measurements. Maximum likelihood estimation (MLE) is superior to LLE but requires knowledge of the probability distribution function of the SDF estimator. To this end one can exploit the fact that the probability distribution function of a periodogram about the its true mean is well approximated by a χ_D distribution. With an hypothesized true mean SDF defined by a small set of parameters, the parameters can be adjusted to maximize the likelihood that the periodogram was generated by the parameterized SDF. Furthermore, algorithms that adjust parameters to maximize likelihood can use functions of the defining parameters being adjusted to improve performance. Recognizing that correlation between turbulent strength and spectral index estimates is an intrinsic measurement property, error minimization is particularly important. A modified MLE procedure is presented that provides robust initiation and good two-component power law parameter estimates.

Plain Language Summary This paper evaluates power law parameter estimation procedures that are routinely used to characterize intermediate-scale ionospheric structure. An intrinsic correlation between turbulent strength and a large-scale power law index is identified. A modified maximum likelihood procedure is introduced to minimize the parameter errors.

1. Introduction

The principal metric for characterizing ionospheric structure is the spectral density function (SDF), which is formally the expectation of the intensity of a spatial Fourier decomposition of the structure. Ionospheric structure is highly elongated along the direction of the Earth's magnetic field, whereby stochastic variation is manifest only in planes that intercept field lines. Structure models project the two-dimensional structure onto measurable one-dimensional SDFs. Model development has been stimulated by recent physics-based high-resolution equatorial plasma bubble simulations Yokoyama (2017) and by new propagation theory results Carrano and Rino (2016). The equatorial plasma bubble simulations can be used to measure the intermediate-scale structure directly. The propagation theory results relate measured one-dimensional scintillation intensity SDFs to the path-integrated SDFs that generated the scintillation. In effect, the propagation diagnostics can be related directly to equivalent path-integrated structure models.

Because the structures are assumed to be static, conversions of measurement-specific time series to scan distance can be employed for model-data comparisons. Knowledge of the probe motion and structure drift is sufficient for in situ diagnostics. Knowledge of the location and motion of a reference coordinate system is necessary for propagation diagnostics in addition to the structure drift. Either way, the scaling and geometric transformations can be absorbed in an effective velocity such that

$$y(t) = v_{\mathrm{eff}}(t - t_0). \tag{1}$$

Consequently, only spectral analysis of spatially varying data segments needs to be considered.

Finally, by hypothesizing a parameterized analytic SDF form, the structure classification problem is reduced to estimating a small number of defining parameters. The two-component power law model

$$\Phi(q) = C_s \begin{cases} q^{-\eta_1} & for\ q \le q_0 \\ q_0^{\eta_2-\eta_1} q^{-\eta_2} & for\ q > q_0 \end{cases}, \tag{2}$$

where q is the spatial wavenumber in radians per meter is sufficient for characterizing intermediate-scale ionospheric structure. A two-component SDF functionally similar to (2) was introduced by Carrano and Rino (2016) to characterize the path-integrated phase SDF, which is not directly measurable. A compact theory was developed to predict the scintillation intensity SDF as a function of the path-integrated phase parameters. Here we consider direct estimation of power law parameters. The notations C_s and η_n are used to distinguish the in situ parameters from the propagation diagnostic parameters C_p and p_n.

If the theoretical SDF is a multicomponent power law, the simplest approach to power law SDF parameter estimation exploits logarithmic transformation of the spectral estimates. The procedure was used to analyze in situ data from the C/NOFS satellite (Rino et al., 2016). Wavelet-based estimators were used in part to identify homogeneous data segments and also because wavelet estimators are well matched to power law processes. The following correlation between the estimated η_1 and C_s and parameters was noted in the C/NOFS study:

$$\eta_1 = -0.02(C_s dB - C_0 dB). \tag{3}$$

The notation $C_s dB$ means $10\log_{10}(C_s)$. The $C_s dB - \eta_1$ correlation has also been observed in propagation diagnostics (Livingston et al., 1981; Rino et al., 1981).

Linear least squares estimation (LLE) is attractive because it requires no knowledge of the estimator statistics. Furthermore, it is well matched to power law SDFs, which are linear when applied to log-SDF versus log-frequency presentations, as already noted. However, it is well established that improved error performance can be achieved with maximum likelihood estimates (MLEs). However, MLE estimators achieve their performance improvement by using knowledge of the probability density function (PDF) of the estimator. For periodogram spectral estimators the PDF is known to follow χ_D statistics for *any* well-behaved homogeneous process.

There has been a progression of estimation procedures from LLE to MLE, which is well illustrated in the papers by Vaughan (2005, 2010) and Barret and Vaughan (2011). However, the correlation represented by (3) is an intrinsic property of estimated power law parameters; however, they are obtained. Moreover, although wavelet-based estimators are more accurate than periodogram estimators at higher frequencies, errors rapidly build up in the low-frequency range. The frequency dependence of the wavelet error distribution exaggerates the $C_s dB - \eta_1$ correlation. In light of these findings this paper reviews and extends power law parameter estimation procedures.

2. Spectral Analysis Theory Summary

Estimating parameters that define the SDF of a power law processes begins with an SDF estimate. Periodogram-based spectral estimation is well established for this purpose. The periodogram of the data sequence, $F_k = F(k\Delta y)$, for $k = 0, 1, \cdots, N-1$ is defined as

$$P_n = \frac{1}{N}\left|\hat{F}_n\right|^2, \tag{4}$$

where

$$\hat{F}_n = \sum_{k=0}^{N-1} F_k \exp\{-\mathrm{i}nk/N\} \tag{5}$$

is the discrete Fourier transform. From the relation

$$\frac{1}{N}\sum_{k=0}^{N-1} F_k^2 = \frac{1}{N}\sum_{n=0}^{N-1} P_n, \tag{6}$$

it follows that

$$\frac{1}{N}\sum_{k=0}^{N-1}\left\langle F_k^2\right\rangle = \int \Phi(q)\frac{dq}{2\pi}, \tag{7}$$

where the angle brackets denote expectation and $\Phi(q)$ is the SDF.

A standard procedure is used to generate realizations of F_k, namely,

$$F_k = \sum_{n=0}^{N-1}\sqrt{\Phi(n\Delta q)\Delta q/(2\pi)}\zeta_n \exp\{\mathrm{i}nk/N\}, \tag{8}$$

where$\Delta q = 2\pi/(N\Delta y)$ and ζ_n is a zero mean Gaussian process with the white noise property:

$$\left\langle \zeta_n\zeta_n'\right\rangle = \begin{cases} 1 \text{ for } n = n \\ 0 \text{ for } n \neq n' \end{cases}. \tag{9}$$

Substituting (8) into (5), it follows that

$$\left\langle |\hat{F}_n|^2\right\rangle = \Phi(n\Delta q)\Delta q/(2\pi), \tag{10}$$

and from (7)

$$\langle P_n\rangle N\Delta q/2\pi = \Phi(n\Delta q), \tag{11}$$

whereby a properly scaled periodogram is an unbiased estimate of the SDF. Although real processes have features generated by Fourier-component phase correlations, idealized realizations defined by (8) provide well-defined uniform statistics for exploring relations determined by the statistical structure.

Now consider the average

$$y = \frac{1}{M}\sum_{l=1}^{M}\hat{\Phi}_n^{(l)}, \tag{12}$$

where $\hat{\Phi}_n^{(l)}$ is a scaled periodogram estimate of a process with SDF Φ_n. By construction, F_k and $\hat{F}_n$ are Gaussian random processes. For Gaussian random processes the summation of M intensity measurements has a known distribution:

$$P(y) = \frac{y^{M-1}\exp\left\{-y/\left(\Phi_n/M\right)\right\}}{\left(\Phi_n/M\right)^M\Gamma(M)}. \tag{13}$$

As described in Appourchaux (2003), the complex process that generates the realizations has 2 degrees of freedom per realization, which is accommodated in (13). From (13) the moments, $\langle I^m\rangle$, and the fractional moments, $F_m = \langle I^m\rangle / \langle I\rangle^m$, can be computed:

$$\langle I^m\rangle = \frac{\left(\Phi_n/M\right)^m\Gamma(M+m)}{\Gamma(M)} \tag{14}$$

$$F_m = \Gamma(M+m)/\Gamma(M)/M^m. \tag{15}$$

The first and second moments, $< y > = \Phi_n$ and $\sqrt{\langle y^2\rangle - < y >^2} = \Phi_n/\sqrt{M}$, completely define the statistics of $\hat{\Phi}_n$ in terms of Φ_n. The fractional moments for $M = 1$ reduce to $F_m = m!$.

In the following analysis ideal realizations will be used. However, the statistics of real data deviate significantly from Gaussian. Even so, experience and analysis, for example, Kokoszka and Mikoschb (2000), show that the Gaussian results apply more broadly. Figure 1 is a plot of the PDF of y/Φ, which represents the scaled periodogram error relative to the mean. The Gaussian distribution, which is the large-M limit, is overlaid in red. The plot shows that for $M < 10$ there is a significant difference between the most probable value, denoted by the red pentagram, and unity mean. Averaging the periodogram estimates brings the most probable value closer to the desired true mean.

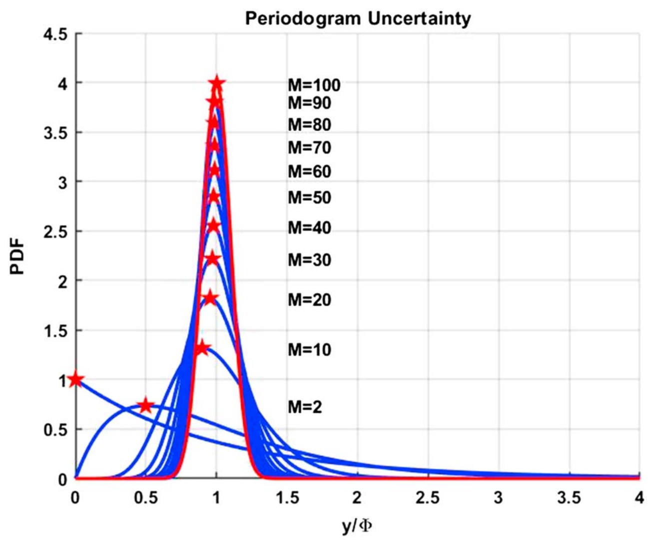

Figure 1. Probability distribution function (PDF) of y/Φ_n (blue) with Gaussian limiting form overlaid (red).

3. Wavelet-Based Spectral Estimation

A complete treatment of wavelets can be found in the text books by Mallat Mallat (2009) or Strang and Borre (1997). Wavelets measure structure scale, s, as a function of the position within a segment as opposed to the Fourier domain frequency, $(2\pi/s)$, which applies to the entire segment. The limitations of position-dependent scale measurements are manifest in the wavelet transformations. The continuous wavelet transformation (CWT) is defined as

$$\begin{aligned} F_w(s,y) &= \int_{-\infty}^{\infty} F(y')\frac{1}{\sqrt{s}}w(\frac{y'-y}{s})\,\mathrm{d}y' \\ &= \int_{-\infty}^{\infty} s\hat{F}(q)\hat{w}(sq)\exp\{iqy\}\frac{\mathrm{d}q}{2\pi}. \end{aligned} \tag{16}$$

The Fourier transform relation is typically used to evaluate the CWT numerically. Wavelets have the following defining properties:

$$w(s) = 0 \text{ for } |s| > 1/2 \tag{17}$$

$$\int_{-1/2}^{1/2} w(s)\mathrm{d}s = 0 \tag{18}$$

$$\int_{-1/2}^{1/2} |w(s)|^2\,\mathrm{d}s = 1 \tag{19}$$

$$\int_{-\infty}^{\infty} |\hat{w}(q)|^2\,\frac{\mathrm{d}q}{q} < \infty. \tag{20}$$

The final property ensures that the CWT is invertible. At each wavelet scale the CWT is a formally a convolution with a wavelet with finite support over the supported scale range.

The discrete wavelet transform (DWT) extracts only octave-spaced wavelet scale estimates at $s = \Delta y 2^j$ for $j = 1, 2, \ldots, J$, where J is the largest power of 2 that equals or exceeds N, that is, $2^J \geq N$. Each DWT wavelet is applied to the even number of samples that span the wavelet. The wavelet scale is defined by j with $j = 1$ corresponding to largest scale, which is usually discarded. The number of wavelet contributions varies with the scale index, j. For $j = 2$, $n = 1$ and 2 corresponding to the centers of two half segments. The smallest wavelet scale contributes $N/2$ centered samples. A discrete wavelet contribution requires a minimum of two data samples. The spatial frequency associated with the structure scale, s, is $q = 2\pi/s$. The DWT,

$$d_n^j = \frac{1}{2}\sum_{k=0}^{N-1} F_k \frac{1}{\sqrt{2^{j-1}}} w((k-n)/2^{j-1}), \tag{21}$$

can be evaluated with the same efficiency as the discrete Fourier transform by using an elegant multifiltering operation described in the cited text book references.

Because the wavelet transform is a linear operation applied to a zero mean Gaussian process, d_n^j, like its periodogram counterpart, is a zero mean Gaussian process. Moreover, from the spectral domain form of the CWT it can be shown that

$$\langle F_w(s,y)F_w(s,y+\Delta y)\rangle = \int_{-\infty}^{\infty} \Phi(q)\,|s\hat{w}(sq)|^2 \exp\{iq\Delta y\}\,\frac{\mathrm{d}q}{2\pi}. \tag{22}$$

From the statistical homogeneity assumption it follows that $\left\langle \left|d_n^j\right|^2 \right\rangle$ is independent of n. The wavelet scale spectrum, as introduced by Hudgins Hudgins et al. (1993), is a summation over the contributing wavelet estimates at each scale; formally,

$$S_j = \frac{1}{2^{j-1}}\sum_{n=1}^{2^{j-1}} |d_n^j|^2. \tag{23}$$

10.1029/2018RS006709

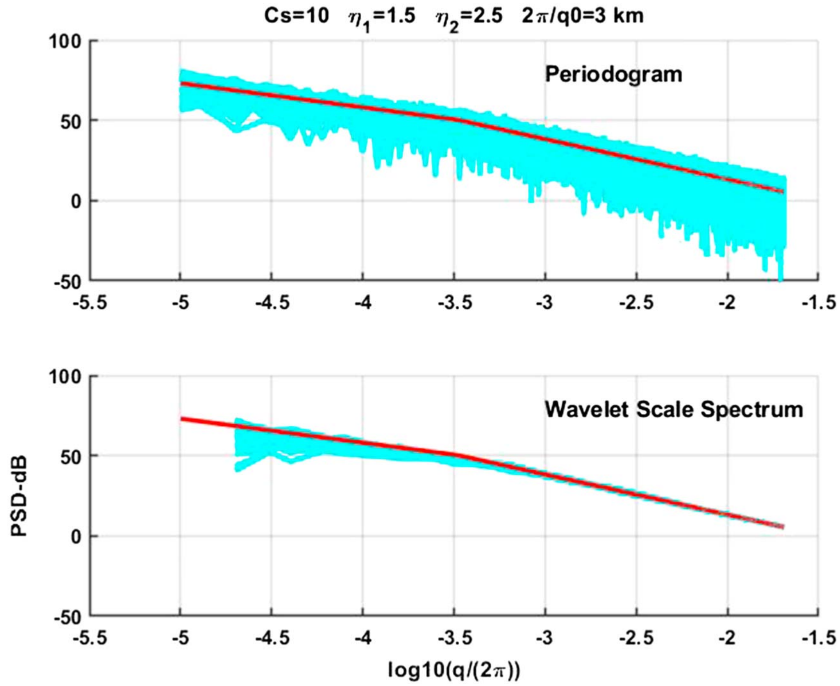

Figure 2. Periodogram upper frame (cyan) and scale spectrum lower frame (cyan) estimates from two-component power law SDF realizations. The solid red curves show the initiating SDF. PSD = power spectral density; SDF = spectral density function.

Upon substituting (2) into (22), it follows that

$$\left\langle \left| d_j \right|^2 \right\rangle = C_s \begin{cases} B_1(\eta_1, q_0) s^{-\eta_1} & \text{for } s \le q_0 \\ B_2(\eta_2, q_0) q_0^{\eta_2 - \eta_1} s^{-\eta_2} & \text{for } s > q_0 \end{cases}, \tag{24}$$

where

$$B_1(\eta_1, q_0) = 2 \int_0^{q_0} u^{-\eta_1} \, |\hat{w}(u)|^2 \frac{\mathrm{d}u}{2\pi}, \tag{25}$$

and

$$B_2(\eta_2, q_0) = 2 \int_{q_0}^{\infty} u^{-\eta_2} \, |\hat{w}(u)|^2 \frac{\mathrm{d}u}{2\pi}. \tag{26}$$

We will show with examples that $B_1(\eta_1, q_0) \sim B_2(\eta_1, q_0) \sim 1$, which implies that $\left\langle \left| S_j \right|^2 \right\rangle = \Phi_j$. We show that the variance of the wavelet scale spectrum estimates decrease with increasing spatial frequency, but the statistics are distinctly different from the χ_D distribution that applies to sums of independent spectral estimates. Unfortunately, we have no characterization of the wavelet scale spectra PDF.

4. Realization Examples

Realizations defined by (8) have been generated with $N = 4,096$ samples spanning 100 km. The sample interval, $\Delta y = 24.41$ m, and the 100-km extent define the positive spatial frequency range from $\Delta q = 2\pi/(N\delta y)$ to the Nyquist frequency $q = \pi/\Delta y$. The sampling and spatial extent were chosen to be representative of ionospheric diagnostic measurements. Because realizations generated by (8) are zero mean and periodic, there are no end point discontinuities that would otherwise introduce side lobe contamination.

Periodogram estimates defined by (4) and scale spectrum estimates defined by (23) were generated from 1,000 realizations for an SDF with $\eta = 2$ and for a two-component SDF with $\eta_1 = 1.5$, $\eta_2 = 2.5$, and $q_0 = 2\pi/3000$. A constant value $C_s = 10$ was used for all the realizations. The constant value of C_s is not restrictive because realizations can be scaled without changing the underlying statistics. For the DWT computation a folded replica of the realization is used to eliminate discontinuities in the last contributing wavelet. Any edge contamination is confined to the wavelet contributing to the largest segment distance.

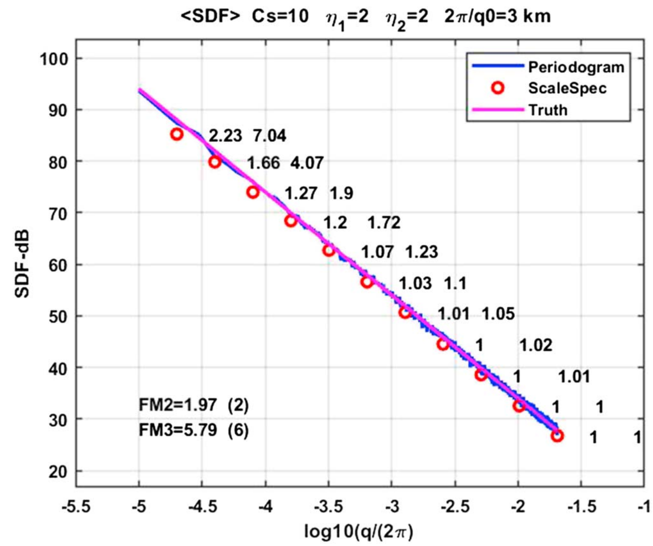

Figure 3. Summary statistics for single power law with $\eta = 2$. SDF = spectral density function.

Figure 2 summarizes the scaled periodogram and scale spectrum estimates for the two-component realizations. The overlaid cyan curves in the upper frame are the 2,047 scaled periodogram estimates spanning the resolved spatial frequency range. The overlaid cyan curves in the lower frame are 11 of the 12 octave-spaced scaled scale spectra estimates, starting with the second resolved scale. The solid red curves are the defining theoretical SDFs. There appears to be less periodogram fluctuation about the mean in the low-frequency range, which is a consequence of the decreasing number of contributing logarithmically spaced frequency samples. We will show that the periodogram fluctuation statistics about the mean are identical at all frequencies. This is in sharp contrast to the wavelet scale spectrum estimates, which have very small variation at the higher frequencies. The scale spectrum error progressively increases to complete uncertainty at the lowest-resolved spatial frequency.

To explore the statistics of the periodogram and scale spectra SDF estimates, 100-realization averages were used to compute the means and the second and third fractional moments. The results are summarized in Figures 3 and 4. Because the periodogram measures are frequency independent, only the average values over the frequency ranges are shown together with the expected theoretical values in predicted by (15) in parentheses. As already noted, there is no complementary PDF model for the wavelet scale spectra. The measured second and third fractional moments are listed next to the average scale spectra samples plotted as red circles. The wavelet fractional moments decrease rapidly to near unity with increasing frequency, which quantifies the observation that wavelet scale spectra estimates are much more certain at the higher frequencies. However, the moments differ significantly from χ_D, where $D = 2N_j$, which would be expected for averaged independent spectral estimates. All the measured moments are nearly identical for the single- and two-component realizations.

5. Logarithmic Transformation

Because of the linear dependence of the logarithm of power law segments on the logarithm of frequency, it is natural to base estimates of the defining power law parameters on logarithmic transformations of spectral estimators. Log-linear least squares estimation (LLE) has been analyzed and reported in a paper by Vaughan (2005). The blue curve in Figure 5 is the average of 100 estimates of $\log_{10}\left(\widehat{\Phi}_n\right)$ versus $\log_{10}(q/(2\pi))$ for the $\eta = 2$ SDF. Aside from the −2.48-dB bias, which can be predicted and removed as shown by Vaughan (2005),

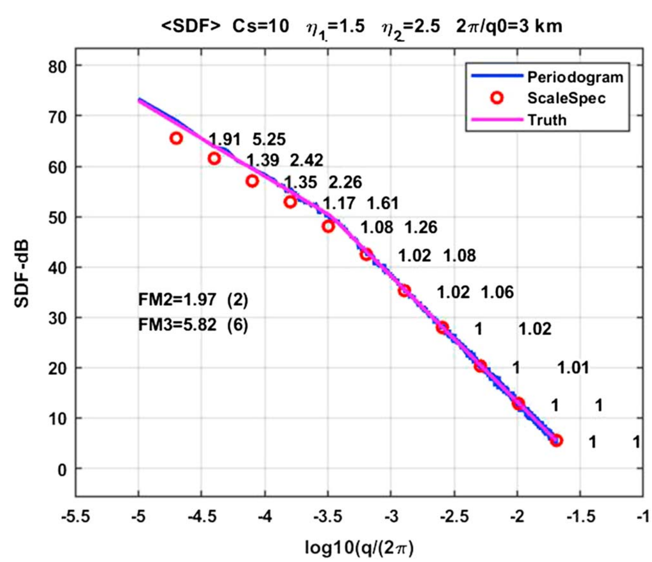

Figure 4. Summary statistics for two-component power law. SDF = spectral density function.

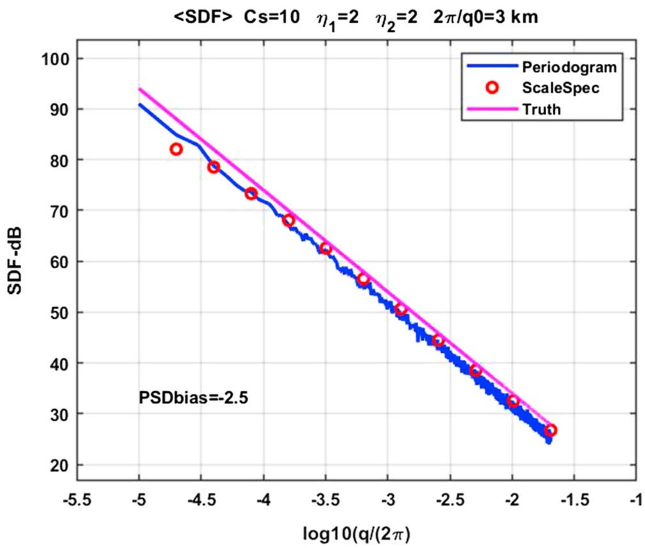

Figure 5. Mean of logarithm of spectral estimates for $\eta = 2$. SDF = spectral density function.

the results suggest that LLE should recover the C_s and η parameters. The wavelet scale estimates (red circles) show negligible bias at large frequencies, with a progressive increase to a larger bias than the log periodogram estimate at the lowest frequency.

Figure 6 summarizes three sets of LLE estimates. The blue circles are derived from periodogram LLE estimates, which are in agreement with Vaughan (2005), although in Figure 6 the bias has not been removed. The cyan circles are derived from scale spectra estimates over the full scale range. The scale spectra results have a smaller bias, but larger uncertainty. However, knowing that the scale spectra uncertainty increases with decreasing frequency, the highly uncertain estimates can be eliminated. The red circles show the scale spectra results derived from scale spectra estimates constrained to the more certain large-scale range. The constrained LLE results with scale spectra are comparable to the periodogram estimates.

The distinguishing characteristic of all the LLE estimators is the correlation of the *CsdB* and η estimates. Formally, the uncertainty ellipse is rotated and displaced from its the true value. The blue line is the least squares fit to the unconstrained periodogram estimates. The log-linear correlation perfectly reproduces the correlation found in the C/NOFS data reported in Rino et al. (2016) and other LLE-based estimates. This shows that the ubiquitous coupling regularly observed in LLE estimates is a measurement artifact, not a characteristic of the structure generation process.

If the measurement objective is to estimate the defining power law parameters, it is necessary to have enough measurements to identify the uncertainty ellipse, whereby the center can be estimated and any known bias corrected. However, if that many independent samples are available, reducing the uncertainty before applying LLE is more effective. This is illustrated in Figure 7. The upper frame repeats the periodogram results shown in Figure 6 for reference. The second and third frames show the improvements realized with LLE $M = 2$ and $M = 10$ preaveraged periodogram estimates. Averaging scale spectra estimates does not improve the results, evidently because the low-frequency errors are not reduced significantly.

The larger challenge is accommodating two-component power law processes, which introduces two-more unknowns. The scheme that was used to analyze the C/NOFS data reported in Rino et al. (2016) applied two LLE

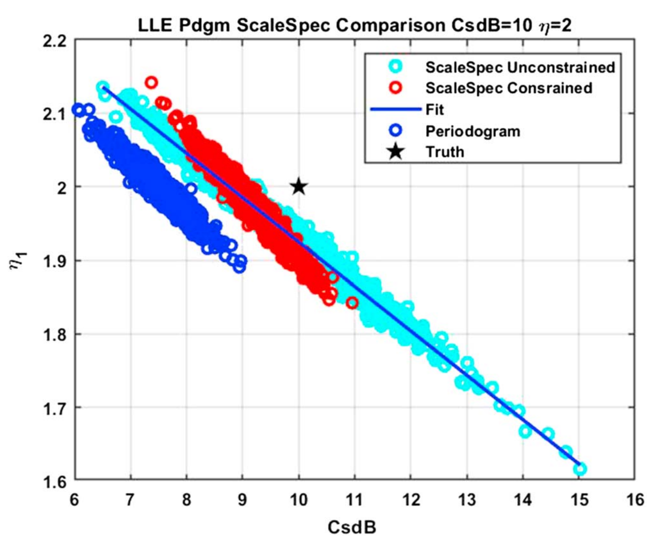

Figure 6. Scatter diagrams of power law log least squares parameter estimates from periodogram (blue) and scale spectra estimates for a single-component $\eta = 2$ power law unconstrained (cyan) and constrained (red). The solid line is a least squares fit to the scale spectra estimates. LLE = linear least squares estimation.

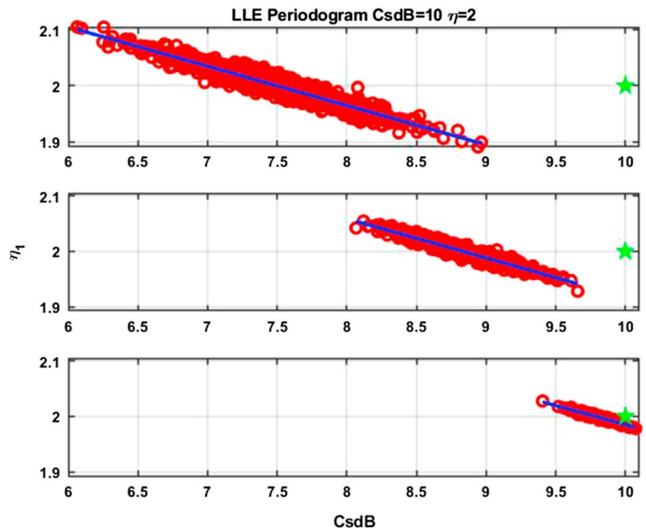

Figure 7. Scatter diagrams of power law parameters derived with LLE applied to $M = 1$), (nonaveraged) $M = 2$, and $M = 10$ preaveraged periodogram estimates. LLE = linear least squares estimation.

fits to partitions with increasing break points. The smallest overall LLE was selected. The problem with this approach, in retrospect, is that it captures and exaggerates the *CsdB*-η correlation.

6. Irregularity Parameter Estimation

Irregularity parameter estimation (IPE) as a generic procedure adjusts a parametric representation of an SDF to *match* a periodogram measurement. This requires a goodness-of-fit measure. Following the progression from LLE to MLE, the initial IPE procedure described in Carrano and Rino (2016) used the LLE measure

$$\epsilon^2(\hat{\Phi}_n|\Phi_n) = \frac{1}{N}\sum_n \left(\log\hat{\Phi}_n - \log\Phi_n\right)^2, \tag{27}$$

where $\hat{\Phi}_n$ represents the periodogram estimate, Φ_n represents the parameterized theoretical model, and N is the number of frequency samples. In a later paper Carrano et al. (2017) revised the IPE procedure to use MLE based on the χ_D model. Here we implement the MLE procedure for estimating two-component power law parameters as an extension of the single-component procedure described and demonstrated in Vaughan (2010) and Barret and Vaughan (2011).

To briefly review the formalism, we let $P(\widehat{\Phi}_n^{(M)}|\Phi_n)$ represent χ_D as defined by (13) with y replaced by $\hat{\Phi}_n$ and Φ replaced by Φ_n. The probability of observing a sequence of independent SDF estimates is $\prod_n P(\widehat{\Phi}_n^{(M)}|\Phi_n)$. Logarithm transformation converts the product to the summation:

$$\begin{aligned}\Lambda(\widehat{\Phi}_n^{(M)}|\Phi_n) &= -\log\prod_{n=1}^{N} P(\widehat{\Phi}_n^{(M)}|\Phi_n)\\ &= \sum_{n=1}^{N}\Big[M(\widehat{\Phi}_n^{(M)}) - M\log(M\widehat{\Phi}_n^{(M)}/\Phi_n)\\ &\quad + \log(\widehat{\Phi}_n^{(M)}) + \log\Gamma(M)\Big].\end{aligned} \tag{28}$$

A maximum likelihood estimate (MLE) is obtained by adjusting the defining Φ_n parameters to minimize (28), which maximizes the likelihood that Φ_n generated the realization.

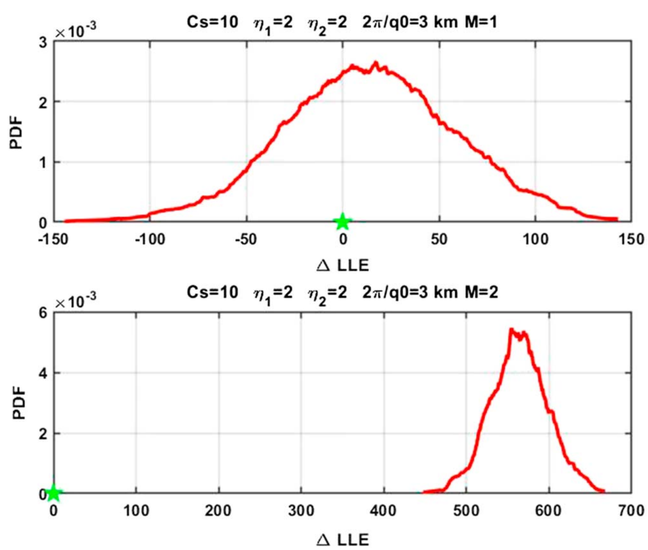

Figure 8. Offset $\Delta\Lambda$ histograms for single power law realizations with $M = 1$ (upper frame) and $M = 2$ (lower frame). PDF = probability distribution function; LLE = linear least squares estimation.

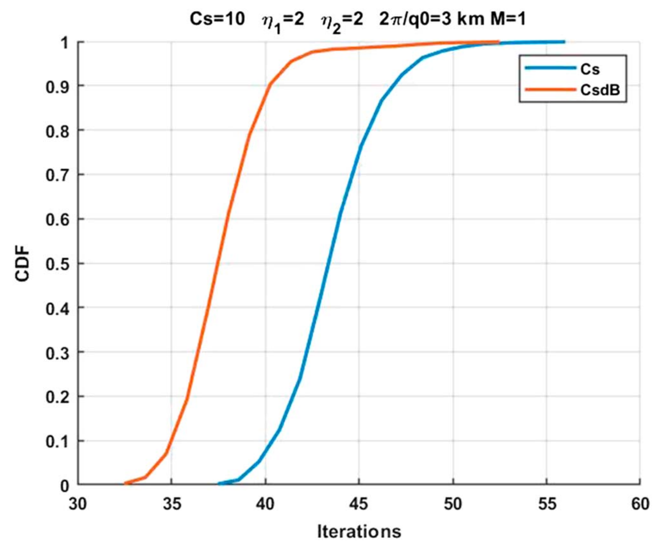

Figure 9. Comparison of Nelder-Mead iterations to convergence with varying C_s and $C_s dB$. CDF = cumulative distribution function.

What remains is to establish a procedure for minimizing (28). For a single-component power law, the parameters that minimize (28) can be computed analytically. Moreover, the statistical theory establishes bounds on the covariance matrix of the MLE parameter estimates. Indeed, covariance calculations by Barret and Vaughan (2011) confirm the C_s-η correlation. For multiple parameter minimization there is a well-established *simplex* method generally referred to a the Nelder-Mead algorithm (Olsen & Nelsen, 1975). As one would expect, the Nelder-Meade algorithm is acutely sensitive to the behavior of the function being minimized as a function of the defining parameters. Indeed, initiating a search with the correct minimum parameters initiates a search, which effectively verifies the parameters. Convergence criteria are also a concern. These issues are discussed in Barret and Vaughan (2011).

We follow Barret's procedure, but note that one has some latitude in determining how the object function $\Delta\Lambda$ is minimized. For example, the algorithm can vary either C_s or the logarithm of C_s. Given the log-linear relation between the turbulent strength and the power law index, one might expect better convergence by varying *CdB*. Either way, the difference between the log-likelihood prior to minimization and the log-likelihood for the true SDF is introduced as a measure of log-likelihood uncertainty:

$$\Delta\Lambda = \Lambda(\hat{\Phi}_n^{(M)}|\Phi_n^T) - \Lambda(\Phi_n^T|\Phi_n^T), \tag{29}$$

where the T superscript indicates the true realization SDF. Figure 8 shows a comparison of $\Delta\Lambda$ histograms for the single power law realizations with $M = 1$ and $M = 2$. Because Λ is minimized for each $\hat{\Phi}_n^{(M)}$ estimate, the negative values in the upper frame of Figure 8 have no particular significance. Consistent with Figure 1, Figure 8 shows that averaging as few as two SDF estimates significantly reduces the $\Delta\Lambda$ variation. The $\Delta\Lambda$ variation for two-component realizations shows identical behavior. With regard to the Nelder-Mead

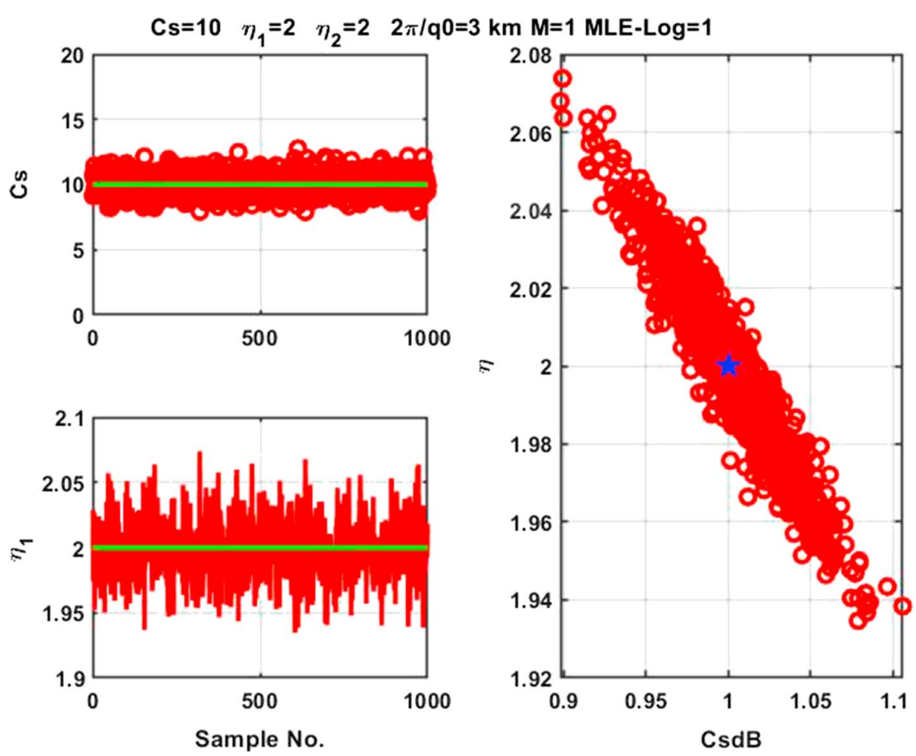

Figure 10. The left frames show maximum likelihood estimation (MLE) parameters for single power law $M = 1$. The right frame shows $\eta - C_s dB$ correlation.

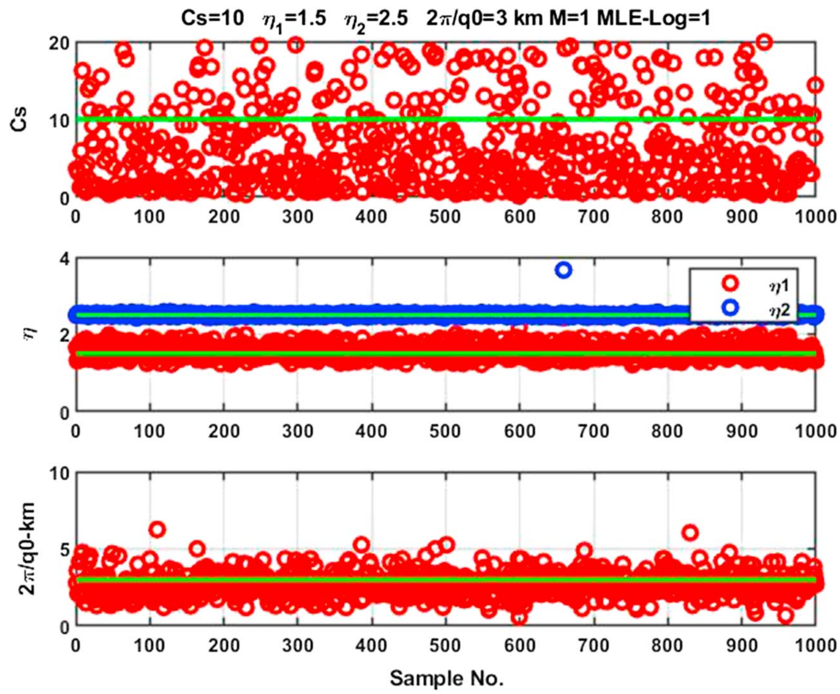

Figure 11. Maximum likelihood estimation (MLE) parameters for $M = 1$ two-component power law realizations.

algorithm, Figure 9 compares the cumulative distributions of the number of iterations to Nelder-Mead convergence with varying C_s and *CsdB*. For these calculations the MATLAB implementation of the Nelder-Mead simplex algorithm was used.

Figure 10 shows the MLE parameters for a single power law with $M = 1$. The Nelder-Mead search was initiated with the LLE estimate. We see that upon comparison to the LLE results, MLE removes the C_s bias and significantly reduces statistical uncertainty. The right frame shows that the C_s-η correlation persists, although the correlation is imperceptible in the summary results. These results are in complete agreement with results reported by Vaughan (2010) and Barret and Vaughan (2011). For the single power law realization processes with no averaging minimizing the object function by varying C_s or *CsdB* has little effect on the uncertainty and $C_s-\eta$ correlation. As an overall check on performance the Nelder-Mead search was initiated with the true parameter values. The differences, including convergence, are imperceptible.

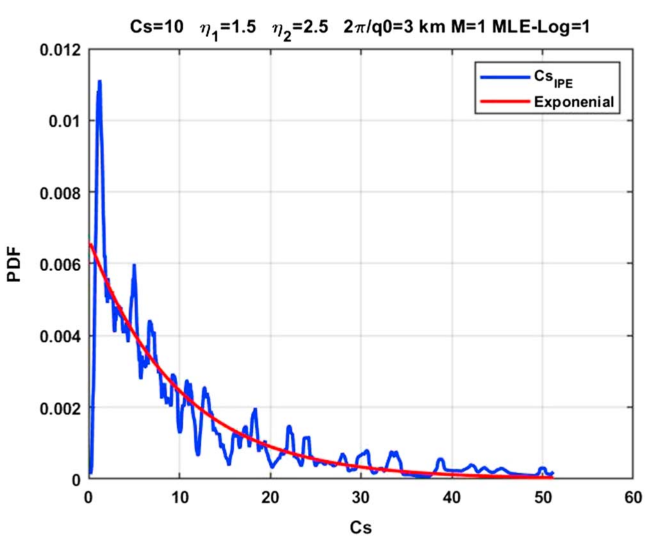

Figure 12. Two-component C_s parameter histogram (blue) with exponential distribution overlaid (red). MLE = maximum likelihood estimation; PDF = probability distribution function.

Two-component power law estimation requires four-parameter initiation. To this end, a midfrequency q_0 estimate is selected, which partitions $\hat{\Phi}_n^{(M)}$ into two contiguous sets. Log-linear least squares estimation is applied to each segment, with a final adjustment to enforce equality at the break scale. For the two-component power law realizations there is a significant improvement in both parameter error reduction and Nelder-Mead convergence when the search is performed on *CsdB*. Figure 11 shows the estimated parameters for $M = 1$. As with the single power law results, the same end result is obtained when the search is initiated with the true parameters. The η_1, η_2, and $2\pi/q$0-km parameters are unbiased.

The C_s parameter estimates are more variable. However, the mean of the estimates is the correct value. To explore this further, Figure 12 shows a histogram of the C_s estimates (blue) with the exponential PDF overlaid in read. Evidently, the C_s fluctuations are capturing the exponential distribution of the periodogram SDF estimate. Figure 13 shows a scatter diagram of the $\eta_{1,2}$ parameter estimates versus $C_s dB$. The $C_s dB$-η_1 correlation persists. However, as with the single power law realizations, the η_1-$C_s dB$ correlation

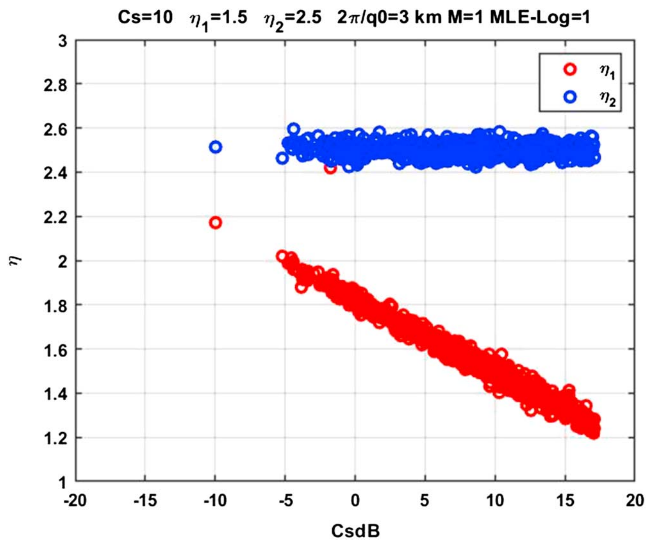

Figure 13. Maximum likelihood estimation (MLE) $\eta_{1,2}$ versus $C_s dB$ scatter diagrams for two-component power law parameters.

is imperceptible in the individual parameter fluctuations. There is no correlation between *CsdB* and the η_2 parameter estimates. Significant improvements are realized with averaging.

7. Discussion and Summary

This paper reviewed LLE and MLE power law spectra parameter estimation using both periodogram and wavelet-based spectral estimators. All of the procedures generate correlated turbulent strength and large-scale spectral index parameter estimates. The correlation has been noted in in situ and remote ionospheric diagnostics but incorrectly attributed to the structuring process. MLE estimation removes biases and significantly reduces statistical errors. Correlation between the *CsdB* and the large-scale index persists. However, the MLE estimate modified to adjust *CsdB* rather than *Cs* reduces the *Cs* and η_1 errors to negligible levels. Even so, correlation can be detected but recognized as intrinsic to parameter estimation.

The fact that using wavelet scale spectra exaggerates the *Cs*-η_1 coupling was not expected. It is well known that the dyadic wavelet scale separation is well matched to the continuous fractal property of power law processes. Our results verify this property, but for parameter estimation scale independence of the error statistics is more important than scale selective error reduction. It the absence of a PDF model for wavelet scale spectra MLE estimation intractable. However, we note that most wavelet-based structure analysis is based on spatial domain structure functions as opposed to spectral domain measures Peter and Rangarajan (2008).

Acknowledgments
The research presented in this paper was undertaken by the authors to correct a miss interpretation in the published C/NOFS analysis. No data were used in the paper. All the results can be reconstructed as described in the paper.

References

Appourchaux, T. (2003). On maximum likelihood estimation of averaged power spectra. *Astronomy and Astrophysics*, *412*, 903–904. https://doi.org/10.1051/0004-6361:20034401

Barret, D., & Vaughan, S. (2011). Maximum likelihood fitting of X-ray power density spectra: Application to high-frequency quasi-periodic oscillations from the neutron star X-ray binary 4u1608-522. *The Astrophysical Journal*, *746*, 9. https://doi.org/10.1088/0004-637X/746/2/131

Carrano, C. S., & Rino, C. L. (2016). A theory of scintillation for two-component power law irregularity spectra: Overview and numerical results. *Radio Science*, *51*, 789–813. https://doi.org/10.1002/2015RS005903

Carrano, C. S., Rino, C. L., & Groves, M. (2017). Maximum likelihood estimation of phase screen parameters from ionospheric scintillation spectra. In *15th International Ionospheric Effects Symposium, Alexandria, VA, May 9-11* (pp. 1–11).

Hudgins, L., Friehe, C. A., & Mayer, M. E. (1993). Wavelet transforms and atmospheric turbulence. *Physical Review Letters*, *71*, 3279–3282.

Kokoszka, P., & Mikoschb, T. (2000). The periodogram at the Fourier frequencies. *Elesiver, Stochastic Processes and their Applications*, *86*, 49–79.

Livingston, R., Rino, C. L., Mcclure, J. P., & Hanson, W. B. (1981). Spectral characteristics of medium-scale equatorial *F* region irregularities. *Journal of Geophysical Research*, *86*(A4), 2421–2428.

Mallat, S. (2009). *A wavelet tour of signal processing: The sparse way*. Amsterdam: Elsevier, Inc.

Olsen, D. M., & Nelsen, L. S. (1975). The Nelder-Mead simplex procedure for function minimization. *Technometrics*, *17*(1), 46–51.

Peter, A. M., & Rangarajan, A. (2008). Maximum likelihood wavelet density estimation with applications to image and shape matching. *IEEE Trans Image Process*, *17*(4), 458–468.

Rino, C. L., Carrano, C. S., Groves, K. M., & Roddy, P. A. (2016). A characterization of intermediate-scale spread F structure from four years of high-resolution C/NOFS satellite data. *Radio Science*, *51*, 779–788. https://doi.org/10.1002/2015RS005841

Rino, C. L., Tsunoda, R. T., Petriceks, J., Livingston, R. C., Kelley, M. C., & Baker, K. D. (1981). Simultaneous rocket-borne beacon and in situ measurements of equatorial spread F—Intermediate wavelength results. *Journal of Geophysical Research*, *84*(A4), 2411–2420.

Strang, G., & Borre, K. (1997). *Linear algebra, geodesy, and GPS*. Massachusetts: Wellesley-Cambridge Press.

Vaughan, S. (2005). A simple test for periodic signals in red noise. *Astronomy and Astrophysics*, *431*, 391–403. https://doi.org/10.1051/0004-6361:20041453

Vaughan, S. (2010). A Bayesian test for periodic signals in red noise. *Monthly Notices of the Royal Astronomical Society*, *000*, 1–15.

Yokoyama, T. (2017). A review on the numerical simulation of equatorial plasma bubbles toward scintillation evaluation and forecasting. *Progress in Earth and Planetary Science*, *4*, 13. https://doi.org/10.1186/s40645-017-0153-6